Supporting Information

Rapid preparation of Fe coordination structure adjustable ORR catalyst by microwave with a half-wave potential above 0.9 V

Qingtao Wang [a,*], Xia Hu [a], Kai Cui [b], Yanxia Wu [a], Guofu Ma [a], Ziqiang Lei [a],

Shufang Ren [c,*]

a Key Laboratory of Eco-functional Polymer Materials of the Ministry of Education, Key Laboratory of Eco-environmental Polymer Materials of Gansu Province, College of Chemistry and Chemical Engineering, Northwest Normal University, Lanzhou 730070, China

b College of Chemistry and Chemical Engineering, Lanzhou University, Lanzhou, 730000, China

c Key Laboratory of Evidence Science Research and Application of Gansu Province, Gansu University of Political Science and Law, Lanzhou 730070, China

Qingtao Wang: wangqt@nwnu.edu.cn
Shufang Ren: rsf@gsupl.edu.cn

Characterizations: The structure of the samples were tested by PANalytical X'Pert PRO X-ray diffractometer (Cu Kα, λ=1.5418 Å). The morphology of the samples were observed through TEM (FEI Tecnai G2 F30) and SEM (Zeiss ULTRA plus). The aberration-corrected high-angle annular darkfield scanning transmission electron microscopy (HAADF-STEM) images were obtained by using a FEI Titan Cubed Themis G2 300 TEM, equipped with a probe spherical aberration corrector. The XAFS spectra were obtained at the 1W1B station of the Beijing Synchrotron Radiation Facility.

Electrochemical Measurements: All electrochemical evaluations were performed using a three-electrode system controlled by a PGSTAT128N electrochemical station. A glassy carbon rotating disk electrode (RDE) with a diameter of 5 mm was used as the working electrode. Convert all measured potentials to a reversible hydrogen electrode (RHE) potential by the Nernst equation: E (RHE) = E (Hg/HgO) + 0.059 pH + 0.098. An aqueous solution of 0.1 M KOH were used as the ORR electrolyte. The working electrode was manufactured as follows: catalysts (2 mg) were dispersed in a mixture solution of 980 μL DMF and 20 μL Nafion solution (5 wt.%). The mixture was sonicated for 30 min to form a homogeneous catalyst ink. Then, the catalyst ink (10 μL) was dropped on a 5 mm diameter glassy carbon RDE, and dried at room temperature to obtain a working electrode (mass loading about 0.1 mg cm^{-2}). In all linear sweep voltammetry (LSV) electrochemical tests, the ORR measurements were carried out in O_2-saturated 0.1 M KOH solutions at a scan rate of 5 mV s^{-1}. The cyclic voltammetry (CV) experiments were performed in N_2/O_2-saturated electrolyte solutions with a scan rate of 50 mV s^{-1}. The RDE measurement was performed at a scanning rate of 5 mV s^{-1} at different speeds (400-2025 rpm). The number of electrons transferred (n) and kinetic current density (J_K) during ORR was calculated according to the Koutecky-Levich equation:

$$\frac{1}{J} = \frac{1}{J_L} + \frac{1}{J_K} = \frac{1}{B\omega^{\frac{1}{2}}} + \frac{1}{J_K} \qquad (1)$$

$$B = 0.62nFC_0D_0^{2/3}V^{-1/6} \qquad (2)$$

$$J_K = nFkC_O \qquad (3)$$

Where J is the measured current density, J_K and J_L are the kinetic and diffusion limiting current densities, ω is the angular velocity ($\omega=2\pi N$, N is the rotation speed), n is transferred electron number, F is the Faraday constant (96485 C mol^{-1}), C_0 is the bulk concentration of O_2 (1.2×10^{-6} mol cm^{-3}), D_0 is the diffusion coefficient of O_2 in 0.1 M KOH (1.9×10^{-5} cm^2 s^{-1}), and ν is the kinematic viscosity of the electrolyte (0.01 cm^2 s^{-1}) .

Zn-air batteries tests. The assembly of Zn-air battery used polished Zn plate as the anode, Fe_{NC}/Fe-N_5-C coated carbon paper/gas diffusion layer/Ni foam as the cathode (mass loading: 1.0 mg cm^{-2}), and 6.0 M KOH + 0.2 M $ZnCl_2$ as the electrolyte. For comparison, 20 wt.% Pt/C was used to prepare the contrast electrode. All Zn-air batteries were tested under ambient atmosphere at 25 °C with PGSTAT128N electrochemical working station and LANHE battery test system (CT2001A, Wuhan LAND electronic Co. Ltd., China).

Density Functional Theory (DFT) Calculations. First-principles calculations were performed using the Vienna Ab Initio Calculation Software Package [1, 2]. Based on density functional theory, commutative association functional use Perdew-Burke-Ernzerh in Generalized Gradient Approximation. The valence electron wave function is spread out by plane wave, and other electrons are approximated with a frozen core, and the plane wave truncation energy is 400 eV [3]. The computational model uses 7×4×1 supercells, and the Brillouin zone sampling uses a Γ-centric grid. The conjugate gradient minimization algorithm is used in the calculation [4]，The atomic coordinates are structurally optimized so that the force acting on each atom does not exceed 0.05 eV Å^{-1}.

The change of the Gibbs free energy (ΔG) for each elementary step at the zero potential can be written as:

$$\Delta G_{(0)} = \Delta E + \Delta E_{ZPE} - T\Delta S$$

Where E is the energy that can be directly obtained from the DFT calculations. E_{ZPE} is the zero-point energy that can be calculated using $E_{ZPE} = 1/2\Sigma h\nu$, in which ν is the vibrational frequency of a normal mode and h is the Planck constant. S is the entropy that can be calculated as:

$$S(T) = k_B \sum_i \left(\frac{h\nu_i}{k_B T} \frac{1}{\exp\left(\frac{h\nu_i}{k_B T}\right) - 1} - \ln\left(1 - \exp\left(\frac{h\nu_i}{k_B T} - 1\right)\right) \right)$$

k_B and ν_i are the Boltzmann constant and vibrational frequency, respectively.

Supplementary Figures:
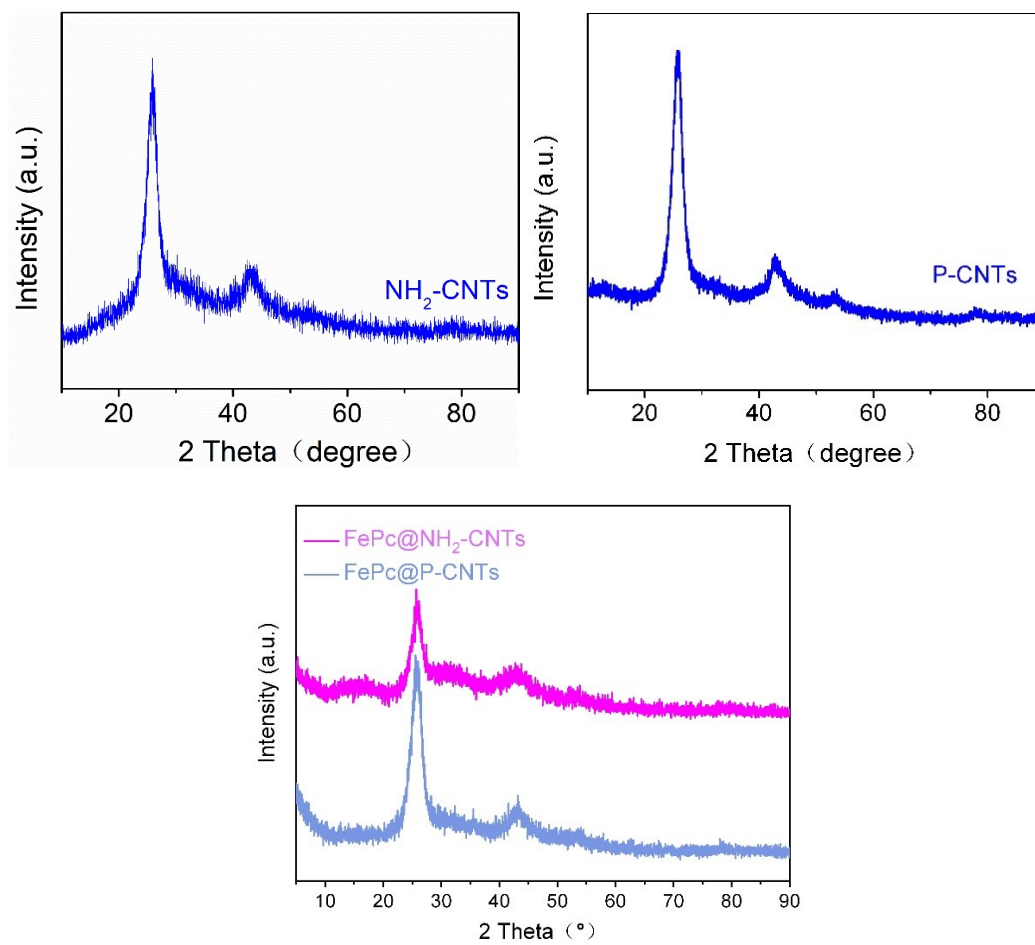
Figure S1. XRD patterns of NH$_2$-CNTs, P-CNTs FePc@NH$_2$-CNTs and FePc@P-CNTs.
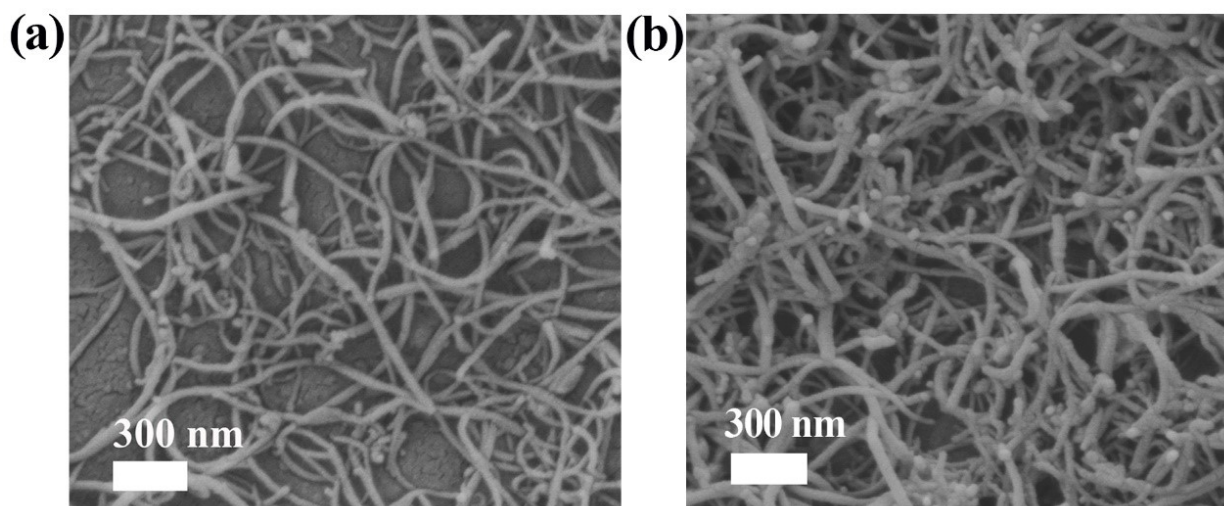
Figure S2. SEM images of (a) Fe$_{NC}$/Fe-N$_5$-C and (b) Fe$_{NC}$/Fe-N$_4$-C.
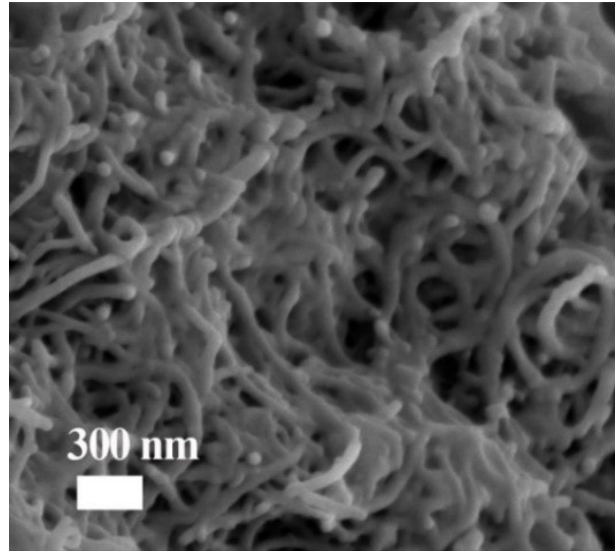
Figure S3. SEM image of NH_2-CNTs.
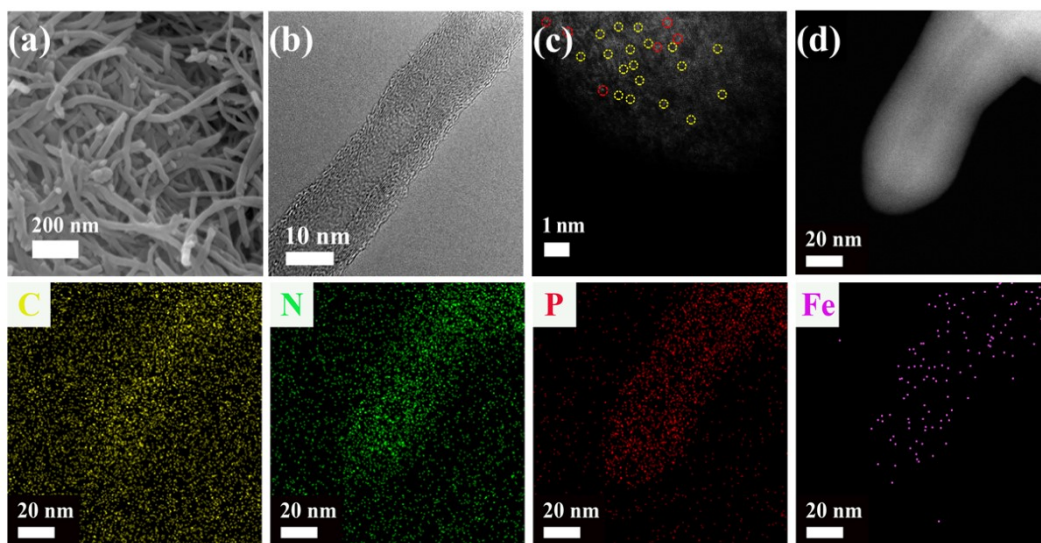
Figure S4. (a) SEM image and (b) TEM image of Fe_{NC}/Fe-P-N_4-C. (c) AC HAADF-STEM image of Fe_{NC}/Fe-P-N_4-C. (d) HAADF-STEM image and elements mapping of C, N, P, and Fe in Fe_{NC}/Fe-P-N_4-C.
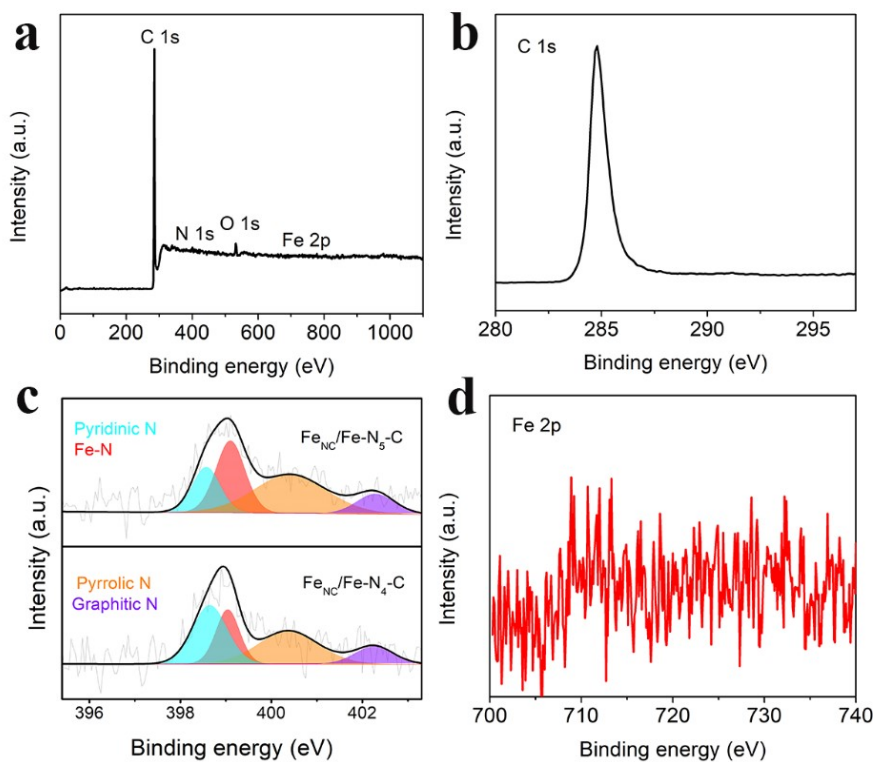
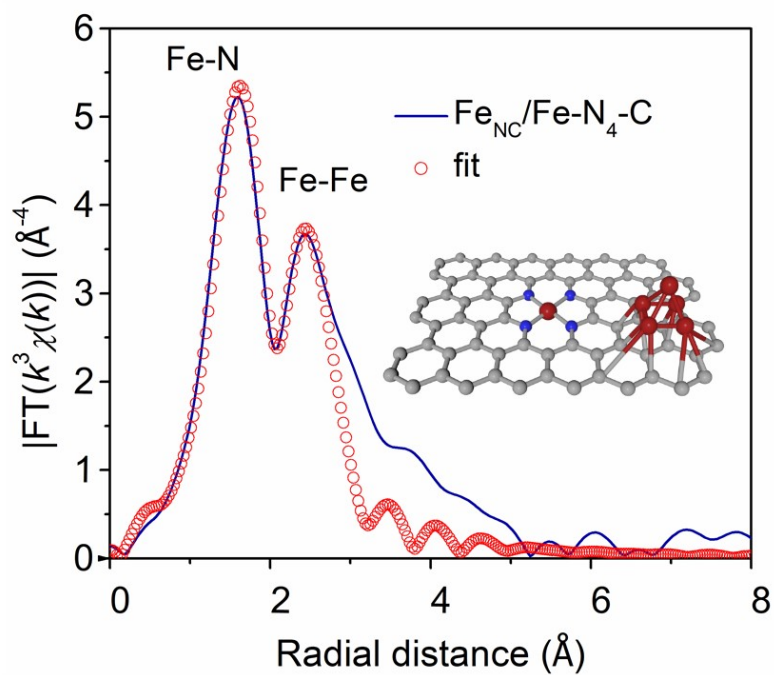Figure S5. XPS analysis of $Fe_{NC}/Fe-N_5-C$. (a) full spectrum, (b) C 1s, (c) comparison of N 1s between $Fe_{NC}/Fe-N_5-C$ and $Fe_{NC}/Fe-N_4-C$, (d) Fe 2p.
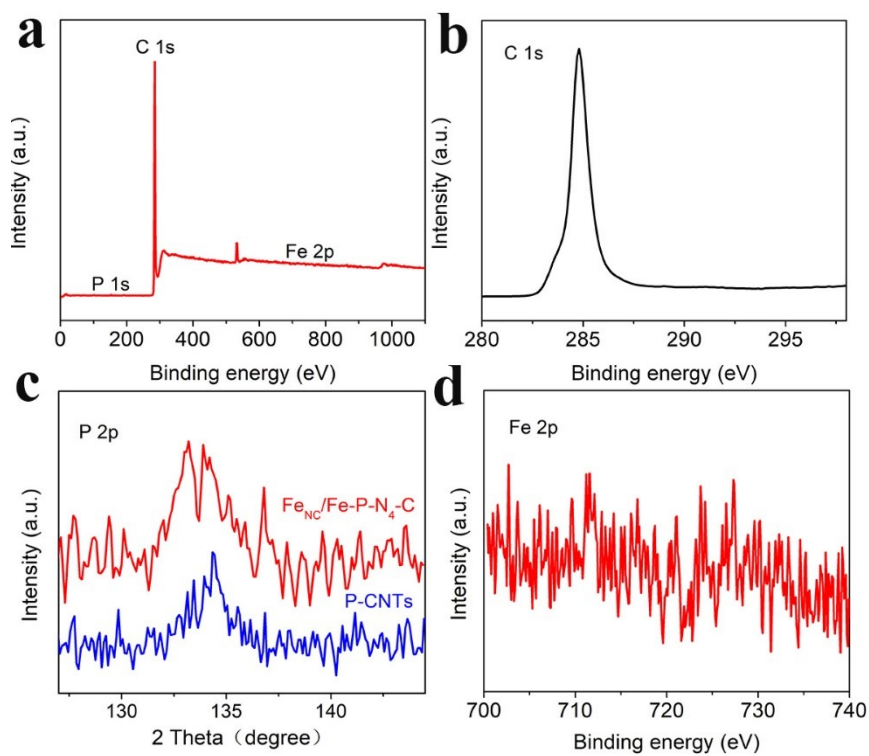
Figure S6. XPS analysis of $Fe_{NC}/Fe-P-N_4-C$. (a) full spectrum, (b) C 1s, (c) comparison of P 2p between $Fe_{NC}/Fe-P-N_4-C$ and P-CNTs, (d) Fe 2p.

Figure S7. The EXAFS curve fitting of $Fe_{NC}/Fe\text{-}N_4\text{-}C$ catalyst in R space. The inset shows the structure diagram on which the EXAFS fitting process is based.
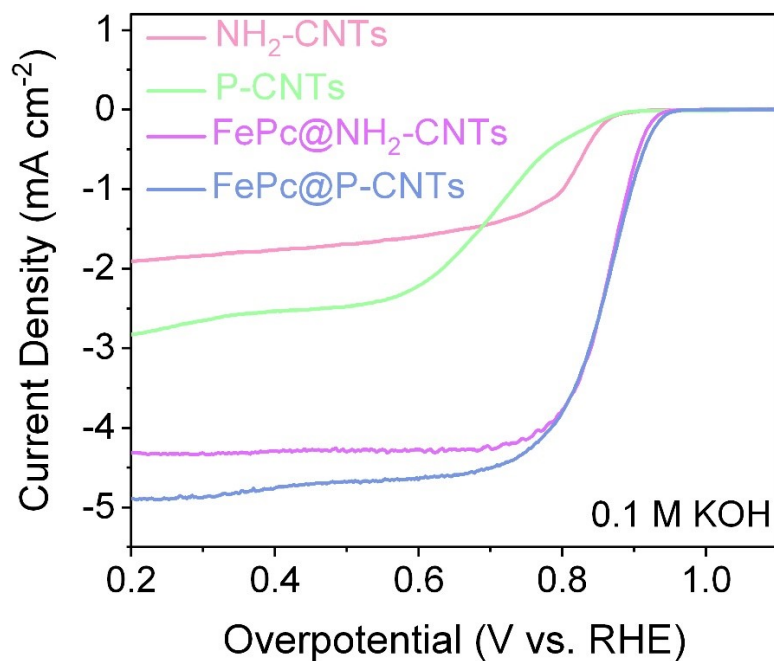
Figure S8. LSV curves of NH_2-CNTs, P-CNTs, FePc@NH_2-CNTs, and FePc@P-CNTs.
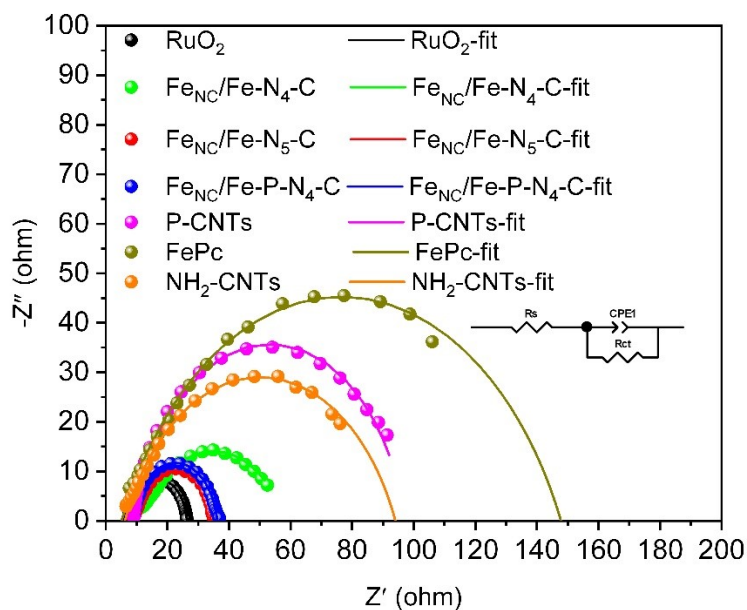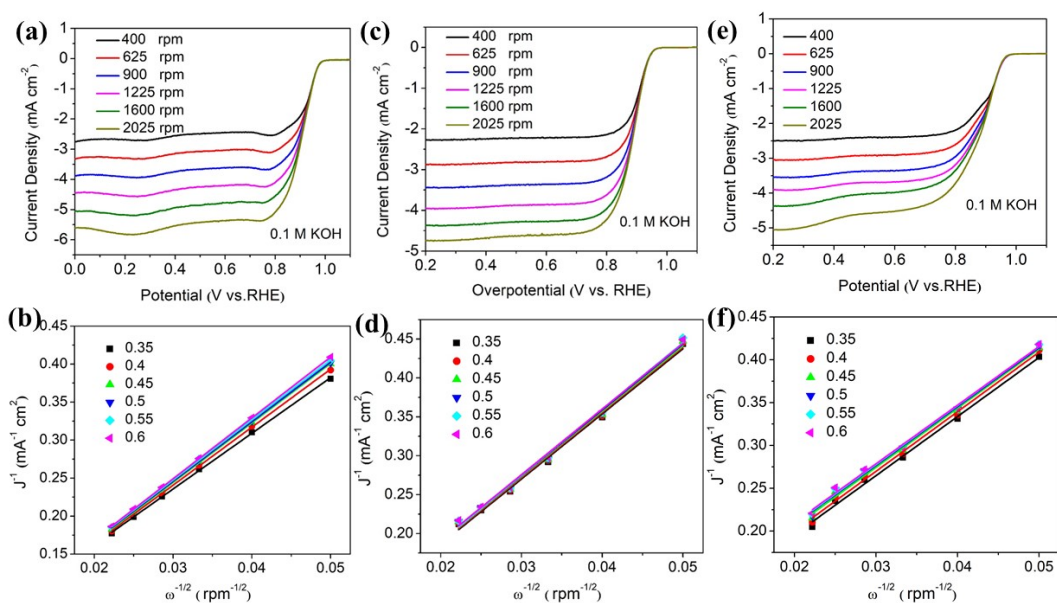
Figure S9. The Nyquist plots of various catalysts.

Figure S10. Rotating-disk voltammograms in 0.1 M KOH at 5 mV s^{-1} and corresponding Koutecky–Levich plots (J^{-1} versus $\omega^{-0.5}$) at different potentials: (a, b) Fe$_{NC}$/Fe-N$_5$-C, (c, d) Fe$_{NC}$/Fe-P-N$_4$-C, and (e, f) Fe$_{NC}$/Fe-N$_4$-C.
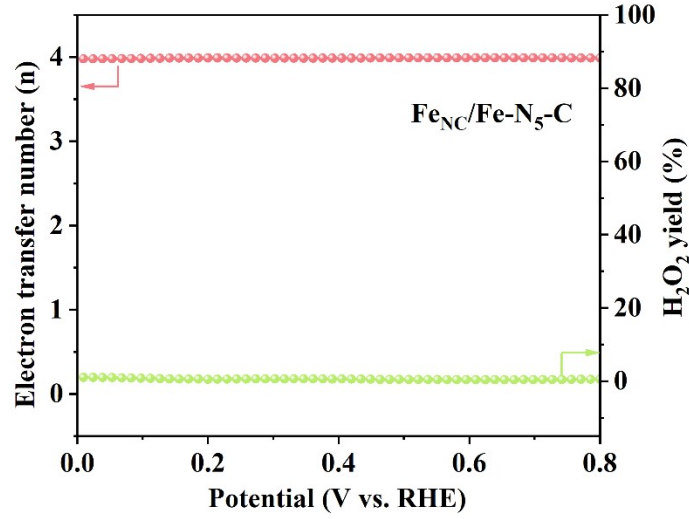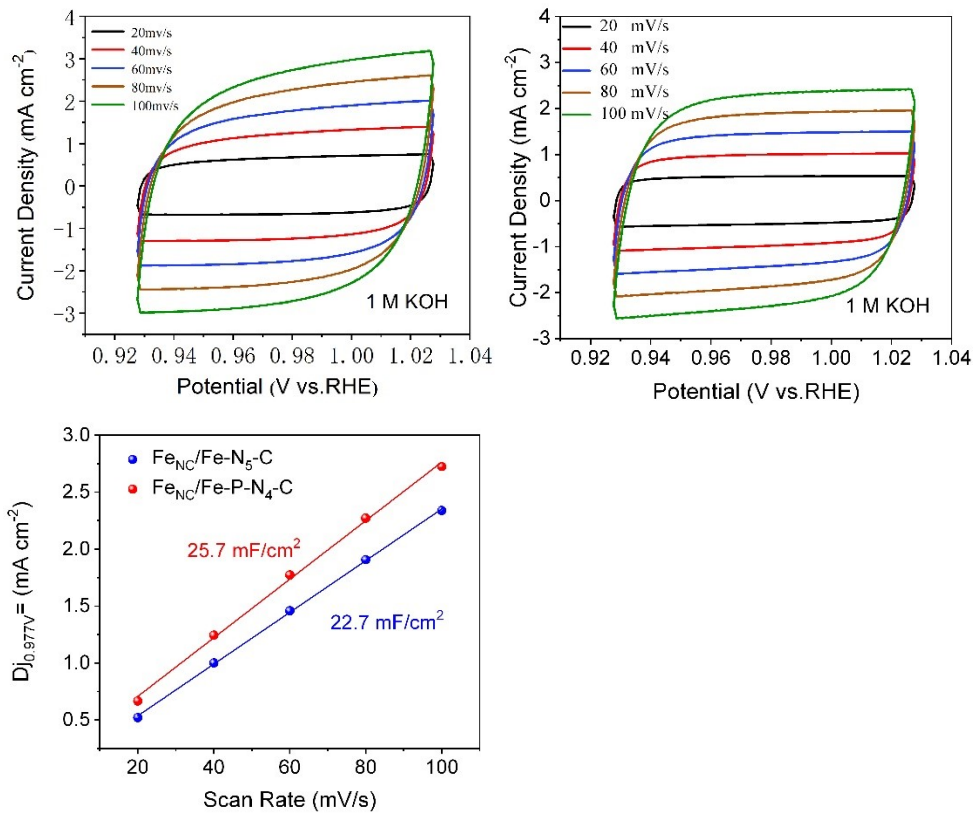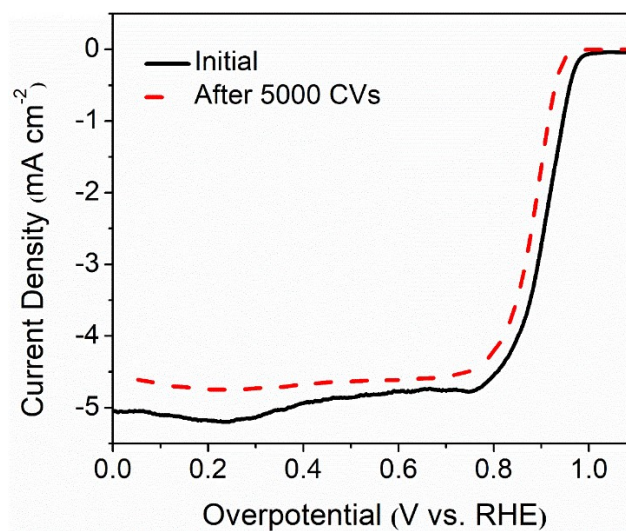
Figure S11. The RRDE results of $Fe_{NC}/Fe-N_5-C$.

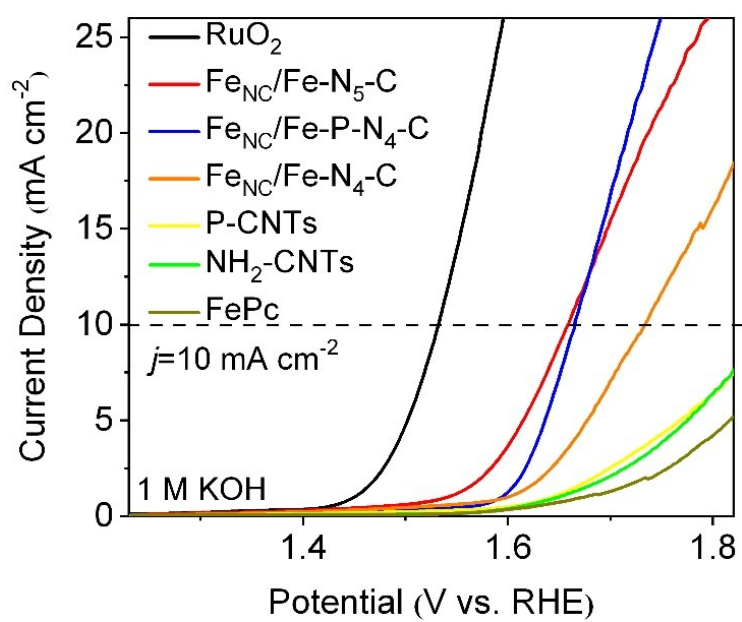
Figure S12. The electrochemical double layer capacitance of $Fe_{NC}/Fe-N_5-C$ and $Fe_{NC}/Fe-P-N_4-C$.

Figure S13. ORR polarization plots for $Fe_{NC}/Fe-N_5-C$ before and after 5000 CV cycles in O_2-saturated 0.1 M KOH.

Figure S14. OER polarization plots for $Fe_{NC}/Fe-N_5-C$, $Fe_{NC}/Fe-P-N_4-C$, $Fe_{NC}/Fe-N_4-C$ and other comparison samples.
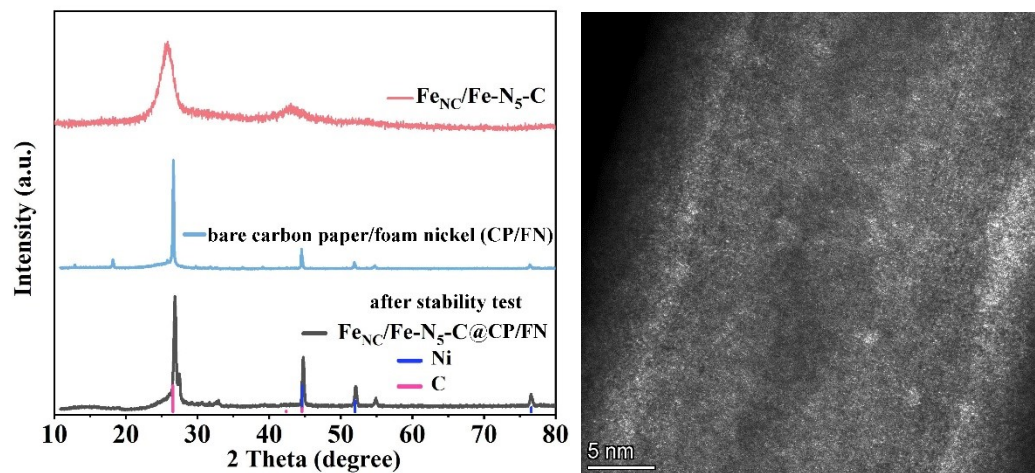
Figure S15. The XRD and AC-HAADF-STEM analysis of $Fe_{NC}/Fe-N_5-C$ after a long-time stability test.
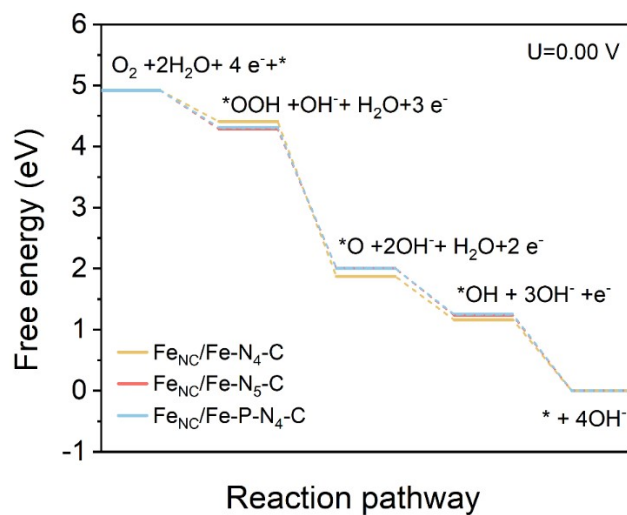
Figure S16. ORR Gibbs free energy diagram of $Fe_{NC}/Fe-N_4-C$, $Fe_{NC}/Fe-P-N_4-C$, and $Fe_{NC}/Fe-N_5-C$ at U= 0 V.
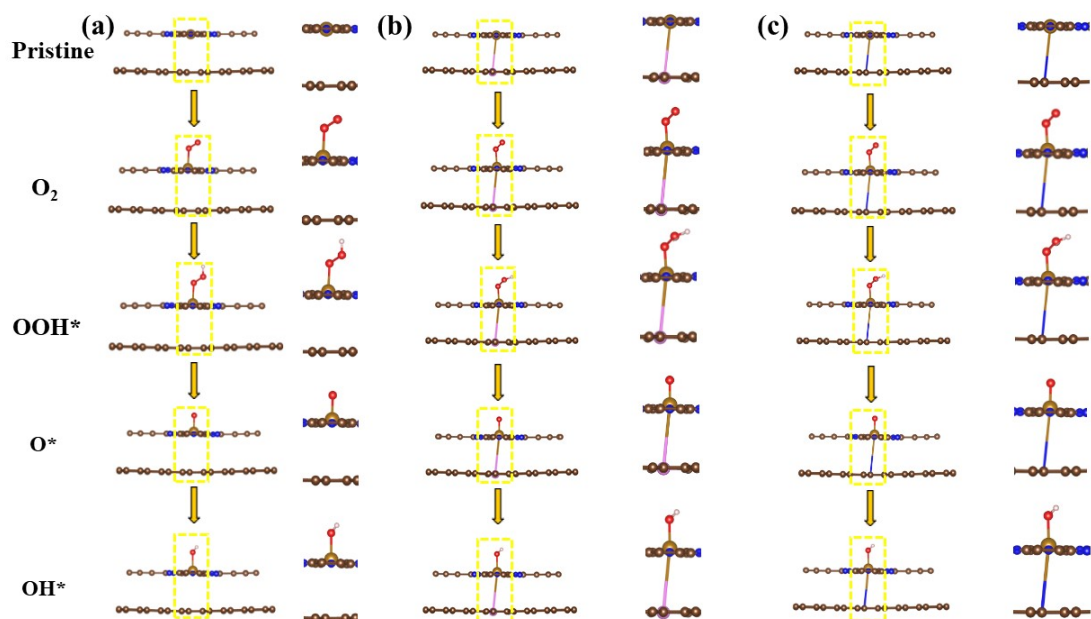
Figure S17. DFT optimized structures (side view) of (a) Fe_{NC}/Fe-N$_4$-C, (b) Fe_{NC}/Fe-P-N$_4$-C, and (c) Fe_{NC}/Fe-N$_5$-C, with adsorbed O_2 and ORR intermediates. The magnified view of the labeled region highlights the catalytic process at 4-electron ORR. (O: Red, Fe: Yellow, C: Brown, N: Blue, P: Pink, H: White).

Table S1. Comparative ORR performance of as-prepared catalyst with other reported Fe single atom-based ORR catalysts.

Catalysts	Metal content (wt%)	E_{onset} (V vs RHE)	$E_{1/2}$ (V vs RHE)	Reference
Fe_{NC}/Fe-N$_5$-C	3.16 (ICP-OES)	0.986	0.906	This work
Fe_{NC}/Fe-N$_4$-C	2.86 (ICP-OES)	0.979	0.864	This work
FePc@CeO$_2$/NSCNF	2.15 (ICP-MS)	1.00	0.890	[5]
Fe-N-C-2	-	0.98	0.81	[6]
Fe3C@NCNTs	-	0.96	0.84	[7]
Fe-SA/NC	0.93 (ICP-OES)	1.10	0.905	[8]
Fe−N−C/GC	1.74 (ICP-OES)	-	0.86	[9]
M-Fe$_2$O$_3$/Fe$_{SA}$@N	1.2 (ICP-OES)	1.05	0.85	[10]
ZIF8@FePMPDA-920	1.25 (ICP-OES)	1.03	0.90	[11]
Fe-N$_5$-LS	2.69 (ICP-OES)	-	0.88	[12]
Fe-N-C-2	4.5 (ICP-MS)	-	0.901	[13]
FeNC-VN	-	0.990	0.902	[14]

Table S2. ICP-OES results of Fe content in catalysts.

Samples	Fe content (wt %)
Fe_{NC}/Fe-N$_5$-C	3.16%
Fe_{NC}/Fe-N$_4$-C	2.86%
Fe_{NC}/Fe-P-N$_4$-C	2.82%

References:

[1] BLöCHL P E. Projector augmented-wave method [J]. Physical review B, 1994, 50(24): 17953.

[2] KOZLOV A N-E S M, VIñES F, ILLAS F. Electronic-structure-based chemical descriptors:(in) dependence on self-interaction and Hartree-Fock exchange [J]. Phys Rev B, 1996, 54: 11169-86.

[3] KRESSE G, FURTHMüLLER J. Efficiency of ab-initio total energy calculations for metals and semiconductors using a plane-wave basis set [J]. Computational materials science, 1996, 6(1): 15-50.

[4] PULAY P. Convergence acceleration of iterative sequences. The case of SCF iteration [J]. Chemical Physics Letters, 1980, 73(2): 393-8.

[5] TAO S, XIANG S, YU Y, et al. Regulating electron region of central Fe atom in iron phthalocyanine by N, S-doped carbon nanofibers as efficient oxygen reduction catalysts for high-performance Zn-air battery [J]. Carbon, 2024, 220.

[6] JIANG Y, XU H, MA B, et al. Polypyrrole derived carbon nanotube aerogel based single-site Fe-N-C catalyst with superior ORR activity and durability [J]. Fuel, 2024, 366.

[7] XU C, GUO C, LIU J, et al. Accelerating the oxygen adsorption kinetics to regulate the oxygen reduction catalysis via Fe3C nanoparticles coupled with single Fe-N4 sites [J]. Energy Storage Materials, 2022, 51: 149-58.

[8] YANG L, ZHU Y, YAO X, et al. Surface-optimized carbon nanocages with tailorable atomic Fe-N4 sites to boost oxygen reduction in long stable zinc-air battery [J]. Energy Storage Materials, 2023, 63.

[9] XING G, ZHANG G, WANG B, et al. Strengthening oxygen reduction activity based on the cooperation of pyridinic-N and graphitic-N for atomically dispersed Fe sites [J]. Journal of Materials Chemistry A, 2023, 11(17): 9493-503.

[10] ZHANG F, ZHU Y, ZHONG Y, et al. Tuning the charge distribution and crystal field of iron single atoms via iron oxide integration for enhanced oxygen reduction reaction in zinc-air batteries [J]. Journal of Energy Chemistry, 2023, 85: 154-63.

[11] ZHOU S, CHEN C, XIA J, et al. 3D Hollow Hierarchical Porous Carbon with Fe-N4-OH Single-Atom Sites for High-Performance Zn-Air Batteries [J]. Small, 2023, 19(48).

[12] XUE D, YUAN P, JIANG S, et al. Altering the spin state of Fe-N-C through

ligand field modulation of single-atom sites boosts the oxygen reduction reaction [J]. Nano Energy, 2023, 105.

[13] TU H, ZHANG H, SONG Y, et al. Electronic Asymmetry Engineering of Fe–N–C Electrocatalyst via Adjacent Carbon Vacancy for Boosting Oxygen Reduction Reaction [J]. Advanced Science, 2023, 10(32).

[14] LYU L, HU X, LEE S, et al. Oxygen Reduction Kinetics of Fe–N–C Single Atom Catalysts Boosted by Pyridinic N Vacancy for Temperature-Adaptive Zn–Air Batteries [J]. Journal of the American Chemical Society, 2024, 146(7): 4803-13.